4-4-2001

Physical properties of Heusler-like Fe2VAl

Ye Feng
Iowa State University

J. Y. Rhee
Iowa State University

T. A. Wiener
Iowa State University

David W. Lynch
Iowa State University, dlynch@iastate.edu

B. E. Hubbard
Cornell University

See next page for additional authors

Physical properties of Heusler-like Fe_2VAl

Ye Feng, J. Y. Rhee,* T. A. Wiener, and D. W. Lynch
Ames Laboratory and Department of Physics and Astronomy, Iowa State University, Ames, Iowa 50011

B. E. Hubbard and A. J. Sievers
Laboratory of Atomic and Solid State Physics, Cornell University, Ithaca, New York 14853-2501

D. L. Schlagel, T. A. Lograsso, and L. L. Miller
Ames Laboratory, Iowa State University, Ames, Iowa 50011

(Received 13 July 2000; published 4 April 2001)

A comprehensive characterization of the compound Fe_2VAl was carried out. Samples grown by arc melting or the Bridgman method have Al and Fe deficiencies of up to 5 at. %. Czochralski-grown samples were Fe rich and Al deficient. X-ray diffraction implies appreciable antisite disorder in all of our samples. Fourier-transform infrared (FTIR) spectroscopy measurements showed that the carrier density and scattering time had little sample-to-sample variation or temperature dependence for near-stoichiometric samples. FTIR and dc resistivity suggest that the transport properties of Fe_2VAl are influenced by both localized and delocalized carriers, with the former primarily responsible for the negative temperature coefficient of resistivity. Magnetization measurements reveal that near-stoichiometric samples have superparamagnetic clusters with at least two sizes of moments. We conclude that in Fe_2VAl, antisite disorder causes significant modification to the semimetallic band structure proposed theoretically. With antisite disorder considered, we are now able to explain most of the physical properties of Fe_2VAl. None of our data suggest heavy-fermion behavior in our samples.

DOI: 10.1103/PhysRevB.63.165109 PACS number(s): 72.15.−v, 61.10.−i, 78.30.Er, 72.15.Rn

I. INTRODUCTION

Fe_2VAl has a number of properties that make it of current interest. Its high resistivity and negative temperature coefficient of resistivity [(TCR), defined as $d(\ln R)/dT$] distinguish it from conventional intermetallic compounds.[1] Yet, contrary to an intermetallic semiconductor, photoemission experiments on Fe_2VAl suggest a reasonable density of states (DOS) at the Fermi level E_F.[1,2] The electronic specific-heat coefficient was also reported to be enhanced.[1,3,4] Despite the presence of Fe, this Heusler alloy does not order ferromagnetically, at least above 4.2 K,[1,5] although some samples show evidence of superparamagnetism (SPM).[5]

As V is doped into the Heusler alloy Fe_3Al with the fcc $D0_3$ structure, no abrupt structural transformation is observed.[1,5] There have been different nomenclatures for the resultant Fe_2VAl to imply structural information. In this paper, we use Fe_2VAl as the name of the stoichiometric compound. FeVFeAl and FeFeVAl are used to indicate the basis along the body diagonal in the $D0_3$ unit cell. In FeVFeAl, V has replaced the Fe which has O_h site symmetry in Fe_3Al, resulting in the cubic $L2_1$ structure. If all the V atoms interchange with the same neighboring Fe atoms in FeVFeAl, the basis becomes FeFeVAl. In fact, FeFeVAl and FeVFeAl are the only two possible $D0_3$ bases in Fe_2VAl.

Several band-structure calculations have been carried out,[6–9] all of which found FeVFeAl to be a nonmagnetic semimetal with a low carrier concentration, about one electron and hole for each 350 unit cells. The density of states (DOS) of FeVFeAl at E_F is about 0.1/eV per f.u.[8] For comparison, the calculated DOS at E_F of FeFeVAl and Fe_3Al are about an order of magnitude larger than that of FeVFeAl.[6] Fe atoms, when placed on the V sites, carry local moments of $1.8\mu_B$ in FeFeVAl,[6] $2.2\mu_B$ in various $Fe_{2+x}V_{1-x}Al$ supercells,[7] and $3.0\mu_B$ in near-stoichiometric Fe_2VAl.[9] These papers, however, gave different opinions on the transport properties and effective-mass enhancement at E_F. Guo *et al.*[6] excluded electron-phonon coupling and expected spin fluctuations in FeVFeAl to be the main cause of the enhanced effective mass, while the negative TCR was due to carrier localization. Singh and Mazin[7] argued that magnetic moments, due to nonstoichiometry and antisite defects, may be responsible for a large effective mass and the complex transport properties from low-density carriers interacting with localized magnetic moments. Weht and Pickett[8] proposed dynamic correlations between holes and electrons as responsible for the resistivity. Bansil *et al.*[9] treated the substitution of Fe with V within the coherent-potential approximation. Recognizing the possibility of samples' having stoichiometry problems and antisite defects, they stated that Fe_2VAl may have the character of a heavy fermion material.

In the following we report a variety of measurements on several samples of Fe_2VAl. Our measurements include composition (by atomic emission spectroscopy), infrared reflectance, x-ray diffraction (XRD), magnetization, and conductivity measurements. None of the samples were exactly stoichiometric due to the preferential loss of Al and Fe in arc melting, and composition gradients in the Bridgman and Czochralski growths. In both FeVFeAl and FeFeVAl, the (111) reflection should be present in the XRD patterns for an fcc lattice, but in all patterns reported here, this reflection is found to be very weak. We modeled the XRD patterns by several possible antisite structures and show that certain site interchanges can account for the weakened (111) peak, although a unique crystal structure cannot be determined. The infrared (IR) spectra can be described accurately by Lorent-

TABLE I. Annealing histories of arc-melted samples.

Samples	Annealing process
A1	At 1273 K (48 h+1 h after cutting) and at 673 K (4 h)
A1-optical	At 1273 K (48 h+1 h after cutting), at 673 K (4 h), and at 673 K (12 h) after polishing
A2-5a, 5b, 5c, 5d	At 1073 K (48 h)
A2-5b-ANN	Sample A2-5b further annealed at 673 K (30 h)
A2-optical, 2b, 2c	At 1073 K (48 h) and at 673 K (17.5 h)
A2-2c-ANN	Sample A2-2c further annealed at 1273 K (1 h) and various anneals below 723 K

zian oscillators representing the IR-active phonons, a single Drude term representing either electrons or holes, and a high-frequency dielectric constant. Magnetization measurements with varying field and temperature confirmed the existence of SPM. The anomalous dc resistivities, although influenced by the magnetic states of the samples, are largely caused by antisite disorder. The Boltzmann formalism of conduction breaks down because of the very short mean free paths of the carriers. Localization due to site disorder, compounded with the low density of carriers in the ordered phase, is responsible for the very large residual resistivity and negative TCR. We found that Fe_2VAl samples grown from the above methods are not single-phase Heusler alloys with the FeVFeAl structure. Their physical properties are the direct result of this deviation.

II. SAMPLES AND EXPERIMENTS

Polycrystalline samples were grown by arc-melting (samples A1 and A2). Samples B1 and B2 were grown by the Bridgman method. We also obtained some single-crystal samples grown by the Czochralski method[10] (sample C). Sample A1 was repeatedly melted on a water-cooled copper hearth with a partial pressure of argon, starting from high-grade Fe, V, and Al. The ingot was kept at 1273 K for two days. It was then cut in half and further annealed at 1273 K for 1 h and 673 K for 4 h. Sample A2 was similarly arc melted and then annealed at 1073 K for two days before cutting. The weight loss was 0.8% for sample A1 and 1.0% for sample A2. Optical samples from A1 and A2 were further annealed for 12–17.5 h at 673 K to remove surface strain due to mechanical polishing. We studied the effect of annealing in arc-melted samples with magnetization and resistivity measurements. The individual histories of samples are listed in Table I.

For the growth of the Bridgman sample, Fe, V, and Al (99.5% or better) were arc melted into buttons then drop cast into a chilled copper mold. The crystal was grown from the as-cast ingot in an alumina crucible. To reduce the Al vaporization during crystal growth the furnace was backfilled to 3.4 atm with argon running through an in-line gettering furnace after the chamber and sample had been outgassed at 773 K. The sample was kept at 1923 K for 1 h to allow thorough mixing before being withdrawn from the hot zone at 5.5 mm/h. Heat treatment of the sample was one week at 1273 K, followed by 4 h at 673 K. Sample B1, from the tip of the single crystal, shows better-defined spots in Laue patterns than sample B2, which was cut from further along the ingot.

Chemical analysis using inductively coupled plasma atomic-emission spectroscopy (ICP-AES) was performed. XRD experiments used Cu K_α I and II lines in Debye-Scherrer geometry. Reflectance measurements were made down to 20 meV at room temperature using a Nicolet FTIR spectrometer, and down to 5 meV at 4 K using a Bomem (FTIR) spectrometer with a 4.2 K Si bolometer detector. The electrical resistivity was measured from 1.8 K to 300 K using a standard four-probe technique. Due to the uncertainty of the bar dimensions and the contact separation, there is an approximate uncertainty of $\pm 10\%$ in the absolute values. dc magnetization was measured using a commercial SQUID magnetometer.

III. CHEMICAL CHARACTERIZATION

The ratios of atomic-emission intensities are tabulated in Table II. In most of the near-stoichiometric samples, an Fe and Al deficiency relative to V is clear. Comparing the total masses estimated from the integrated intensity of atomic emission with those weighed before the ICP-AES experiments, all samples suffer about 2% weight loss in the preparation of solutions, except for sample A1 with its 5% weight loss and some white precipitate in the solution. The precipitate presumably consists of an impurity from the crystal, or Al_2O_3. The vapor pressures of Al and Fe at 1273 K, the annealing temperature, are 10^{-4} and 10^{-6} Torr, respectively, and that of V is negligible. The loss of Al and Fe in arc-melted ingots could very well be from their preferential evaporation in the growth process and in the high-temperature annealing. Assuming there is no loss of V, the above atomic ratios translate to weight losses of 1.6% for sample A1 and 2.6% for sample A2. These ICP-AES atomic ratios tend to overestimate the loss, when compared to the weight loss after the arc-melting growth. We suspect the arc-

TABLE II. ICP-AES results for Fe_2VAl samples. The standard deviations are given in brackets in the first column.

Atomic ratio	A1	A2	B1	B2	C
Fe/2V (3.3%)	0.99	0.96	0.90	0.98	1.05
Al/V (3.0%)	0.95	0.98	0.83	0.99	0.98

melted Fe_2VAl samples were already Fe and Al deficient right after growth. Bridgman sample B1 is off stoichiometry but sample B2 looks reasonable. This difference arises from the interplay of the temperature gradient from the pedestal to the melt, and the convective and diffusive mixing that are particular to the Bridgman method. Although the stoichiometry of sample B1 is quite different from those of the others, we keep it in our study for comparison. The Czochralski sample is Fe rich. This deviation is presumably also from the crystal growth. We regard all samples except B1 and C to be be near stoichiometric. Although Al and Fe deficiencies will cause a shift of E_F, it is considered to be insignificant. Scanning electron microscope studies show that both the polished and unpolished surface of sample A2 are homogeneous within 5 at. %.

IV. POWDER X-RAY DIFFRACTION

In the history of Fe_2VAl characterization, different structures have been proposed, based on powder XRD results. Early research on $FeAl_{1-x}V_x$ (Ref. 11) identified the formation of FeVFeAl through powder XRD and neutron scattering. Few guesses of possible structures were used to settle on this structure. Nevertheless, the agreement between theory and experiment appeared to be excellent. Later, Popiel *et al.*[5] attempted to obtain the occupation-number distribution for every constituent at every site of the $D0_3$ structure from experimental powder XRD. Few details were provided for this complicated process but they concluded that V prefers to be in the FeFeVAl ordering, rather than FeVFeAl. They also noticed that the ratio of structure factors for (111) to (200) reflections decreased throughout the $Fe_{3-x}V_xAl$ series with increasing x, reaching about 0.2 at Fe_2VAl. Structural disorder was suggested. Recently, Nishino *et al.*[1] claimed Fe_2VAl to be FeVFeAl, although diminished (111) and (200) peaks were also reported. Here we present our data and analysis to show that FeVFeAl is not the only crystal structure in Fe_2VAl, and the suppression of the (111) and (200) peaks can be explained by structural disorder.

We used the PowderCell 2.1 program[12] and an experimental lattice constant of 5.761 Å to calculate peak intensities for all structures considered, with a Debye-Waller factor of 0.9 for each atom. In ideal FeVFeAl, the strongest peaks have Miller indices of (220), (422), (400), (200), and (111), shown in Fig. 1. The calculated intensity ratios $F^2_{(111)}/F^2_{(220)}$, $F^2_{(200)}/F^2_{(220)}$, $F^2_{(400)}/F^2_{(220)}$, and $F^2_{(422)}/F^2_{(220)}$ are 0.043, 0.065, 0.133, and 0.229, respectively. Although in our calculations $F^2_{(111)}/F^2_{(220)}$ agrees very well with the calculated and experimental value in Ref. 11, our calculated $F^2_{(200)}/F^2_{(220)}$ is 0.065 instead of the 0.5 reported for both calculations and experiments.[11]

All our experimental XRD profiles (of sample A1, A2, B1, B2, and C) were similar and none showed any unexpected peaks above the 1% detection limit. Measured patterns of samples A2 and B1 are shown in Fig. 1, along with the calculated patterns for FeVFeAl and FeFeVAl. Peak heights were normalized to that of the (220) peak which was given an intensity of 100. All measured spectra show a (111) peak at about $2\theta \simeq 27°$ with strongly suppressed intensity, and a (200) peak slightly reduced from the calculated values for FeVFeAl, at $2\theta \simeq 31°$.

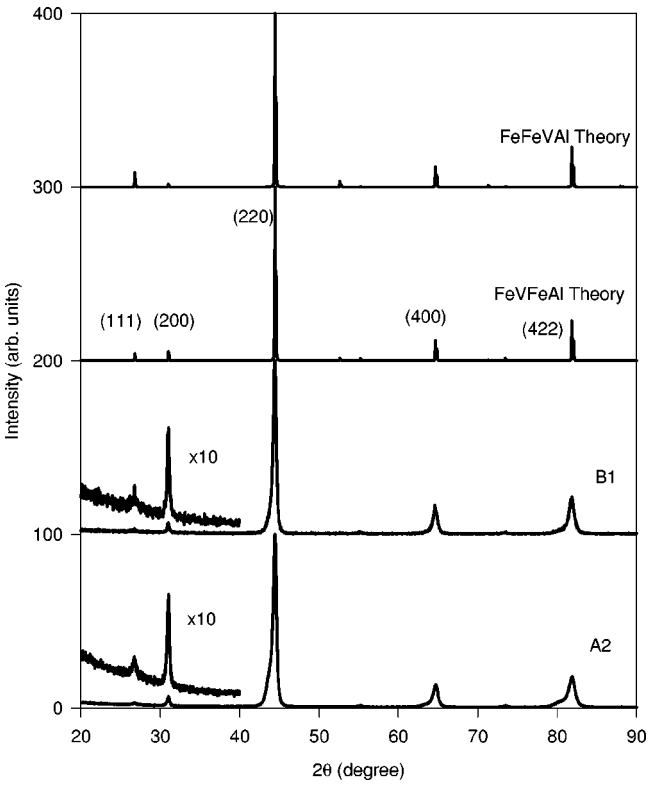

FIG. 1. Powder XRD patterns of Fe_2VAl.

In addition, the patterns from samples A1, A2, B2, and C had shoulders on the low-angle sides of the (220), (400), and (422) peaks, but sample B1 had almost no such shoulder. (Since the ICP-AES analysis showed sample B1 to be chemically different from others, we should note that about 10% chemical disorder may not distort the diffraction pattern noticeably.) These shoulders scaled in intensity with their respective main peaks, indicating a close connection in origin. We also annealed some powder from sample A1 at 673 K for 30 h, and powdered part of the annealed optical sample A2. In both cases, the lower-angle shoulders of the diffraction peaks were no longer visible. Therefore, these shoulders probably originated from the bulk, not from the grinding process. However, the $F^2_{(111)}/F^2_{(200)}$ ratio of sample A1 becomes even smaller after annealing.

We did numerical fitting to our XRD data to obtain relative peak intensities. A fourth-order polynomial was used to fit the background, which was then subtracted. Assuming a Lorentzian line shape for each peak, we acquired the intensity ratios of $F^2_{(111)}/F^2_{(220)}$ and $F^2_{(200)}/F^2_{(220)}$ and tabulated them in Table III. We also used two Lorentzians for the (220) peaks. $F^2_{(200)}/F^2_{(220)L}$ and $F^2_{(200)}/F^2_{(220)H}$ in the table refer to ratios to the shoulders at lower angles and to the main peaks at higher angles of the (220) peaks. It is noted that $F^2_{(111)}$ and $F^2_{(200)}$ scale better with the main peak or the total of (220), rather than with just the shoulder. For all samples except B1, we also found $d_{220,L}/d_{220,H} = d_{400,L}/d_{400,H}$

TABLE III. Experimental XRD intensity ratios with standard deviations in brackets.

Sample	$\frac{F^2_{(111)}}{F^2_{(200)}}$	$\frac{F^2_{(200)}}{F^2_{(220)tot}}$	$\frac{F^2_{(200)}}{F^2_{(220)L}}$	$\frac{F^2_{(200)}}{F^2_{(220)H}}$
A1	0.44(10%)	0.033(3%)	0.11(9%)	0.045(4%)
A2	0.37(5%)	0.032(2%)	0.12(6%)	0.041(2%)
C	0.27(32%)	0.030(7%)	0.091(11%)	0.043(8%)
B2	0.30(18%)	0.048(5%)	0.21(18%)	0.062(8%)
B1	0.33(13%)	0.036(3%)	0.17(18%)	0.045(6%)
A1[a]	0.26(17%)	0.052(5%)	-	-

[a]Powder from sample A1 further annealed at 673 K for 30 h.

$=d_{422,L}/d_{422,H}$, where d_{hkl} is the spacing between planes with Miller index of (hkl).

Since most of the peak ratios roughly agree with the predicted values for FeVFeAl, we assign all our samples to be close approximates to this structure. However, the shoulders and the reduced (111) and (200) intensities require some modification to the structure. Since the FeFeVAl phase enhances the (111) peak relative to the (200) peak (see Fig. 1 and Table IV), its presence does not help explain our XRD profiles. The calculated effect of vacancies did not agree with experiments either. Within the structure of FeVFeAl, reducing the atomic form factor of Al by 10% increased both (111) and (200) intensities with respect to that of the (220), while reducing the Fe form factor increased the (111) intensity and reduced that of the (200).

We consider site-interchange disorder as the possible cause of the weakened (111) peak. Instead of constructing many supercells to model antisite disorder, we treated each lattice site as being statistically occupied. With no indication of a structural transition,[1,5] it is reasonable to assume that the underlying lattice for Fe_2VAl is the $D0_3$ structure, with basis atoms at (0,0,0), $(\frac{1}{4},\frac{1}{4},\frac{1}{4})$, $(\frac{1}{2},\frac{1}{2},\frac{1}{2})$, and $(\frac{3}{4},\frac{3}{4},\frac{3}{4})$. At each basis site, we assumed fractional occupation by Fe, V, and Al in units of $\frac{1}{2}$ atom. With few exceptions, the diffraction intensities for non-half-integer occupancy can be interpolated from those with half-integer occupancy. This choice of quantization reveals the necessary features of the diffraction pattern without extensive calculations. We assumed full stoichiometry for the model structures.

We can categorize the structures by the number of sites with identical occupancy and determine the crystal symmetry, or space group, through site-symmetry analysis.[13] There are 13 possible atomic arrangements that keep the proper stoichiometry, all listed in Table IV. When two atoms *A* and

TABLE IV. All the theoretical structures considered for antisite disorder and the ratios of powder pattern intensities. In the ''Atomic arrangement'' column the sequence is $(0,0,0)$-$(\frac{1}{4},\frac{1}{4},\frac{1}{4})$-$(\frac{1}{2},\frac{1}{2},\frac{1}{2})$-$(\frac{3}{4},\frac{3}{4},\frac{3}{4})$. **FA** = Fe/Al, **FV** = Fe/V, and **VA** = V/Al. See the text for explanations.

Space group	Atomic arrangement	$\frac{F^2_{(111)}}{F^2_{(200)}}$	$\frac{F^2_{(111)}}{F^2_{(220)}}$	$\frac{F^2_{(200)}}{F^2_{(220)}}$
$Pm(-3)m$[a]	Fe-**VA**-Fe-**VA**$^{\alpha}$*	0.000	0.000	0.065
$Pm(-3)m$[a]	**FV-FA-FV-FA**$^{\beta}$*	0.000	0.000	0.021
$Fd(-3)m$	**FV-FA-FA-FV**	∞	0.021	0.000
$Fd(-3)m$	**VA**-Fe-Fe-**VA**$^{\gamma}$	∞	0.064	0.000
$Fm(-3)m$	Fe-V-Fe-Al$^{\delta}$ [b]	0.650	0.043	0.065
$Fm(-3)m$	**FV**-Al-**FV**-Fe	3.750	0.080	0.021
$Fm(-3)m$	**FA**-V-**FA**-Fe*	0.270	0.006	0.021
$F(-4)3m$	Fe-Fe-Al-V[c]	4.020	0.085	0.020
$F(-4)3m$	**FV-FV**-Al-Fe	1.520	0.060	0.040
$F(-4)3m$	**FA-FA**-V-Fe	8.050	0.024	0.003
$F(-4)3m$	Fe-**VA-FV-FA***	0.071	0.003	0.040
$F(-4)3m$	Fe-**VA-FA-FV**	13.000	0.040	0.003
$F(-4)3m$	**FV-VA-FA**-Fe	∞	0.043	0.000
72.6% of α and 27.3% of γ		0.37	0.017	0.047
70.9% of β and 29.1% of δ		0.37	0.013	0.034

[a]Its proper lattice constant is half of 5.761 Å.

[b]This is the FeVFeAl phase mentioned in the text.

[c]This is the FeFeVAl phase mentioned in the text.

B share the same site, the label *A*/*B* is used. We calculated all the peak intensities and normalized them. Because of a sum rule,[11] the intensities of the (220), (400), and (422) peaks of these 13 structures were identical, hence not useful for discrimination.

Only four types of structures can yield a reduced $F^2_{(111)}/F^2_{(200)}$. They are starred in Table IV. Any one, or several, of these can mix with FeVFeAl or other phases with high $F^2_{(111)}/F^2_{(200)}$ values, to produce a powder pattern close to the experimental one. They may also produce the observed shoulders because of the slightly different lattice parameters of the phases involved. The XRD profile is then a weighted average of that of each phase. The bottom two rows in Table IV list two phases that can give an $F^2_{(111)}/F^2_{(200)}$ of 0.37, the average of samples A1, A2, and B2.

So far we have established antisite structural disorder as the probable reason for the distorted XRD patterns and that annealing at 673 K does not restore the FeVFeAl structure, although the XRD shoulders are reduced or eliminated. We have not yet been able to pinpoint exactly what lattice structure our samples have. The major difficulties are due to the vast number of possibilities for antisite substitutions in a ternary compound and similar scattering form factors of Fe and V. We do not know how much of a role nondiffracting phases, if any, play in the overall picture. It is not surprising to find such large antisite disorder in arc-melted Heusler alloys. XRD of the line-phase compound Fe_3Al revealed a structural disorder of 8%.[14] Mössbauer experiments on Fe_3Al (Ref. 15) and $(Fe_{1-x}V_x)_3Al$ (Ref. 5) with $0 \leqslant x \leqslant 0.6$ confirmed this antisite disorder and showed it persisting over the V alloying process.

V. FTIR RESULTS

Reflection spectroscopy around the plasma edge is well recognized as an accurate measure of carrier density and scattering time for metallic alloys and semiconductors. Typically the dielectric function of metals is composed of a constant ϵ_∞ and contributions from free electrons, phonons, and interband transitions. ϵ_∞ accounts for the contributions from interband transitions at higher energies.

Figure 2 shows the reflectance $R(\omega)$ of samples A1, A2, B1, and B2. (Because of the small size of sample C, we were not able to measure it.) There are two peaks around 0.03 eV and 0.045 eV in all samples. Besides these two peaks, a tiny feature is also seen around 0.04 eV in sample A2, which shifts to lower energies with decreasing temperature. Bridgman sample B1 has an additional peak around 0.06 eV. There is no significant change in $R(\omega)$ of sample A2 from 4 K to 300 K, suggesting similar Drude contributions at all temperatures. Other samples, except B1, seem to have similar carrier densities and scattering times. Recent optical conductivity measurements show that Fe_2VAl has interband transitions peaking at 1.1 eV, with a threshold above the Drude contribution around 0.1 eV.[16,17] We therefore tend to regard the upturn of samples A2 and B2 near 0.08 eV as the onset of interband contributions.

The peaks at 0.03 and 0.045 eV are readily identified as phonon peaks for the following reasons. First, inter-valence-band transitions depend strongly on the available states below and above E_F. At infrared frequencies, the strength of these transitions is strongly influenced by thermal broadening of the Fermi function. If the 0.03-eV peak were due to interband transitions, its intensity and width would have changed significantly when the temperature increases from 4 to 300 K. Optical phonons are, however, much less temperature sensitive. Second, it is not unusual that disorder changes energy eigenstates near E_F thereby altering the frequency, width, or intensity of interband transitions. With all of the phonon peaks aligning in energy and having similar width and intensity (numerically shown in Table V), we believe that both peaks are of phonon origin, not from inter-valence-band transitions. Third, IR radiation excites transverse optical (TO) phonons of certain symmetry at the Brillouin-zone center according to dipole selection rules. Correlation-method[13] analysis applied to FeVFeAl with space group $Fm(-3)m$ results in two doubly degenerate TO modes with $\mathbf{F}_{1u}$ symmetry which are IR active. A third doubly degenerate TO mode has $\mathbf{F}_{2g}$ symmetry and is Raman active but not IR active. In contrast, the FeFeVAl with space group $F(-4)3m$ has three IR active phonon modes with $\mathbf{F}_2$ symmetry. The survival of these phonon features in the presence of structural disorder hints at the dominance of FeVFeAl-like regions in all near-stoichiometric Fe_2VAl samples.

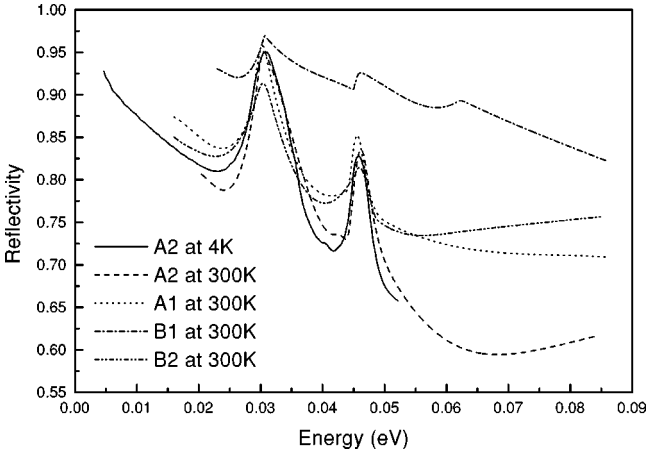

FIG. 2. Far-IR reflectivity of Fe_2VAl.

To understand these spectra quantitatively, we fit each $R(\omega)$ with a sum of a Drude term for the free carriers and Lorentz oscillators for the phonons, together with a constant ϵ_∞. Since only one Drude term was needed to yield a good fit, we will mention only the electronic carriers later on, although holes can as well be present or dominant. Carrier densities and scattering times can be determined, assuming a free-electron mass. Two Lorentz oscillators for samples A1, A2 (at 4 and 300 K), and B2, and three for sample B1, were used in the fitting process. The fit was excellent for all samples except for the minor feature around 0.04 eV in sample A2. The best-fit parameters are listed in Table V. The self-consistency of this fitting is confirmed on sample A2 by comparing the optical conductivity calculated with its best-fit parameters and that from a Kramers-Kronig transformation of its full range $R(\omega)$,[17] in which only $R(\omega)$ below 0.02 eV

TABLE V. FTIR reflectivity fitting parameters.

	A1	A2	A2	B2	B1
Temperature (K)	300	4	300	300	300
Carrier density (10^{20}/cm^3)	5.0	2.0	2.2	3.3	25
Scattering time (10^{-15} s)	7.9	13	11	9.6	7.4
ϵ_∞	184	158	96.3	246	300
Phonon $E1$ (meV)	29.5	29.6	29.7	29.9	30.1
$E1$ width (meV)	0.79	1.1	1.0	2.8	1.5
Phonon $E2$ (meV)	45.3	45.6	45.4	46.0	45.8
$E2$ width (meV)	1.3	1.9	1.8	3.5	1.5
Phonon $E3$ (meV)					61.4
$E3$ width (meV)					4.3
Intensity ratio I_{E1}/I_{E2}	3.9	3.8	4.1	2.7	3.4

and above 22 eV were extrapolated. It should be pointed out that assuming a constant ϵ_∞ is appropriate, as optical conductivity data[16,17] show negligible interband transitions below 0.1 eV.

The fitting results confirmed that the carrier concentrations of samples A1, A2 at 4 and 300 K, and B2 are similar. Their average at 300 K, 3.5×10^{20}/cm^3, agrees with that reported in Ref. 16. The carrier density for sample A2 at 300 K is 0.017 electrons/f.u., comparable to the 0.024 carriers/f.u. (Ref. 7) and 0.006 carriers/f.u. (Ref. 8) predicted from first-principles calculations, although these calculations yielded a renormalized mass for the carriers. It is precisely because of the low density of carriers that the TO phonons are not well screened.

Despite the significantly larger carrier density of sample B1, scattering times for all samples are close to 1.0×10^{-14} s, a typical time scale for metals at room temperature. However, similar scattering times at 4 and 300 K indicate that the scattering is not due to phonons. The product of carrier concentration and scattering time of sample A2 becomes a bit larger from 300 K to 4 K, over which the resistivity increases by almost a factor of 2, as shown in Sec. VII. This fact requires another mechanism of transport besides the conventional conduction described by the Boltzmann formulation to account for the *change* of resistivity over temperature.

Variations in ϵ_∞ come from the dielectric response of valence electrons at higher energies. If we take ϵ_∞ to be 200, an average number in Table V, we can estimate the position of the mean oscillator representing all valence electrons. With 24 valence electrons/f.u. contributing to this oscillation,

$$\omega_0 = \sqrt{\frac{4\pi e^2 n}{m\epsilon_\infty}} = 1.9 \text{ eV}.$$

This is fairly consistent with the position of the main peak of the optical conductivity at 1.1 eV from our spectroscopic ellipsometry.[17]

Lastly, we report that no pseudogap due to electron correlation is observed in this material. Most of the pseudogaps in strongly correlated materials, as in a similar 3*d* metallic alloy FeSi,[18–20] have a strong temperature dependence in reflectivity and optical conductivity. In contrast, our FTIR data for Fe_2VAl show that the concentration and scattering time of free carriers remain nearly constant when the temperature is changed. These electronic carriers do not appear to be influenced by any temperature-dependent correlation mechanisms.

VI. MAGNETISM

The magnetization and magnetostatic susceptibilities of our Fe_2VAl samples are shown in Figs. 3 and 4, respectively. Magnetization was measured up to 5.5 T at 2 K and susceptibility from 2 K to 350 K in 0.1 T for all samples. For

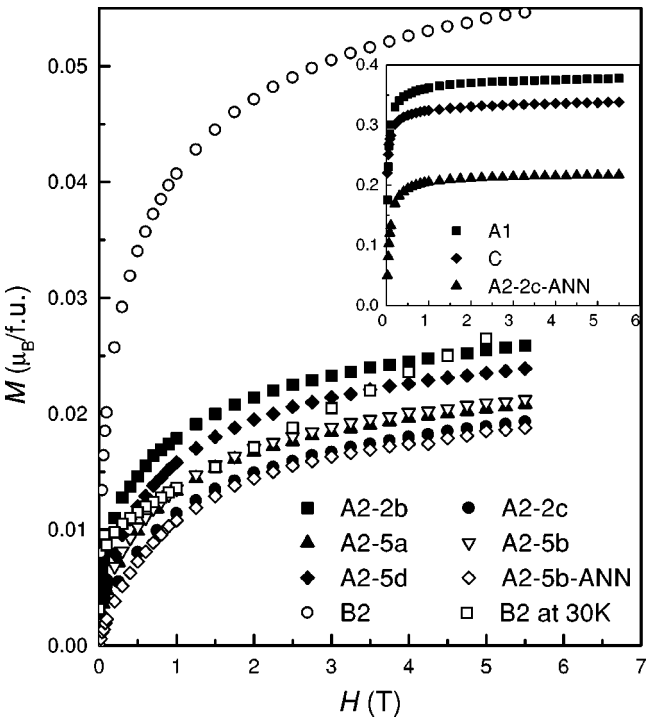

FIG. 3. Magnetization of Fe_2VAl measured at 2 K unless otherwise specified.

sample B2, magnetization was also measured at 30 K.

In Fig. 3, samples A1 and C have saturation moments between 0.3 and $0.4\mu_B$/f.u. Their susceptibilities in Fig. 4 show a magnetic transition temperature near 20 K for sample A1 and 50 K for sample C. The susceptibility of sample A1 above 20 K cannot be explained by the Curie-Weiss law. However, sample C shows clear Curie-Weiss behavior with $\mu_{\text{eff}}=2.8\mu_B$/f.u., $T_C=53$ K, and $\chi_0=-8.5\times10^{-6}$ emu/g, when the susceptibility above 70 K is fitted with

$$\chi=\chi_0+\frac{N_{\text{f.u.}}\mu_{\text{eff}}^2}{3k_B(T-T_C)}.$$

The stoichiometry measurement shows that sample C is iron rich. The excessive Fe atoms might occupy the V or Al sites and form ferromagnetic clusters. Nishino *et al.*[1] have also observed in their resistivity data that a slight increase of iron content in Fe_2VAl does result in ferromagnetism.

All A2-derived samples, even annealed at low temperature, have paramagneticlike magnetizations, as shown in Fig. 3. They do not saturate up to 5.5 T. The magnitude of magnetization of these samples is more than an order of magnitude smaller than those of samples A1 and C. There is no hysteresis observed within the limit of the instruments. The lack of hysteresis is considered a signature of paramagnetism or SPM. Above the blocking temperature T_B, the coupling of SPM clusters is overwhelmed by the thermal energy, giving a magnetization described well by Brillouin functions with large effective magneton numbers. These A2-derived samples all appear to have T_B less than 2 K. The inverse susceptibility data of these samples cannot be explained by the Curie-Weiss law with a single slope at high temperature. Temperature might have an effect on the size of the SPM clusters or the weak interaction among them to cause this complicated magnetic behavior.

Additional annealing at 673 K does not change the magnetic properties of Fe_2VAl in a significant way. The susceptibility of samples A2-5b-ANN is reduced compared to sample A2-5b but with no new features. However, sample A2-2c, after being heat treated at 1273 K for 1 h, shows enhanced susceptibility and magnetization, by a factor of 10 or more. Sample B2 has most of its characteristics similar to those of A2-derived samples, although from the susceptibility a magnetic transition around 10 K is visible. It appears that samples A2-2c-ANN and B2 are in intermediate magnetic states between those of samples A2 and A1. These different states probably have variations in local stoichiometry, the size of SPM clusters, or coupling among them. The field-dependent resistivity, shown later in Sec. VII, also suggests the magnetic transformation from samples A2 and B2 to sample A1.

Popiel *et al.*[5] pointed out the existence of SPM in $Fe_{3-x}V_xAl$ alloys. Across $Fe_{3-x}V_xAl$ they found through Mössbauer and magnetostatic experiments that, with an increase of V content, ferromagnetism weakens and SPM becomes prevalent for $x>0.6$. The reported magnetization of $Fe_{2.2}V_{0.8}Al$ has a similar shape and magnitude as those of our sample A1, albeit a large difference in T_B. (Our susceptibility data are to be multiplied by a field of 0.1 T before comparing with their magnetization data.) They reported the moments of SPM clusters vary from $10\mu_B$ to $10^4\mu_B$, according to different isotherms of magnetization. Fitting our magnetization-vs-field data with one Brillouin function was unsuccessful. Using two Brillouin functions, or even better, two Langevin functions,

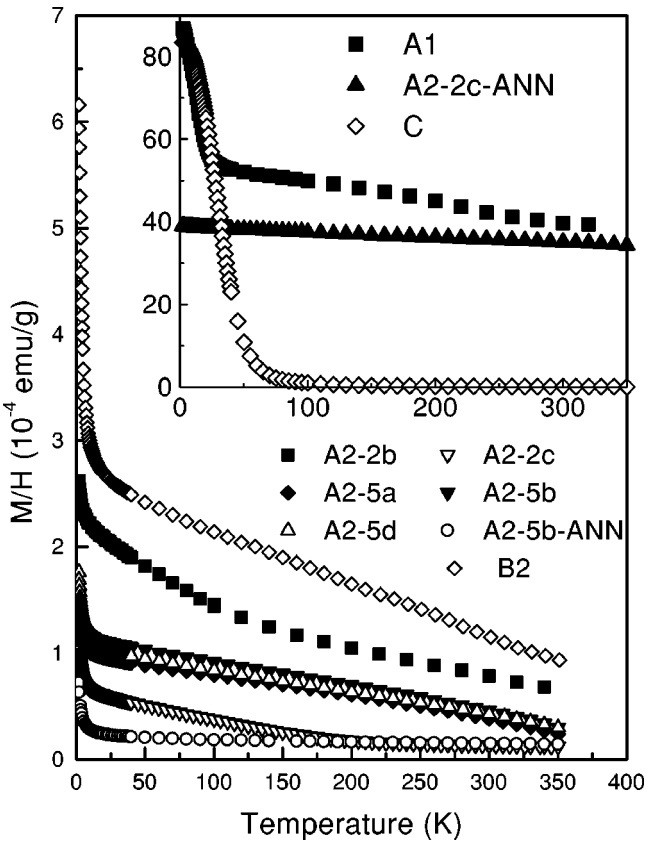

FIG. 4. Susceptibility of Fe_2VAl measured at 1 kG.

$$\frac{\sigma-\sigma_0}{\sigma_S}=a\left[\coth\left(\frac{\mu_1 H}{k_B T}\right)-\frac{k_B T}{\mu_1 H}\right]+(1-a)\left[\coth\left(\frac{\mu_2 H}{k_B T}\right)-\frac{k_B T}{\mu_2 H}\right]$$

we were able to obtain an excellent fit, permitting the extraction of the moments μ_1 and μ_2, their relative fractions, a and $1-a$, the average moment μ_{avg} [$\mu_{\text{avg}}=a\mu_1+(1-a)\mu_2$], the total saturation magnetization σ_S, the field-independent magnetization σ_0, and the cluster density $\sigma_S/\mu_{\text{avg}}$. The results of these fits are listed in Table VI. The field-independent magnetization σ_0, $3\times10^{-3}\mu_B$/f.u., corresponds to a susceptibility of 9×10^{-5} emu/g, which is on the same scale as the high-temperature tail of the susceptibility. Because the Pauli susceptibility is field independent and almost temperature independent, it is probably the cause for the σ_0 and the observed tail.

The concentrations of those two clusters are about constant throughout all A2 samples. Annealing sample A2-5b reduces the moments of both clusters but enhances the clus-

TABLE VI. Results of a two-cluster Langevin fit. Magnetic moments (μ_1, μ_2, μ_{avg}) are in units of μ_B, fraction of clusters (a) that have μ_1 in percentage, magnetizations (σ_0, σ_S) in $10^{-3}\ \mu_B$/f.u., and cluster density (σ_S/μ_{avg}) in per f.u.

Sample	T	μ_1	a	μ_2	μ_{avg}	σ_0	σ_S	$\frac{\sigma_S}{\mu_{avg}}$
A2-2b	2 K	37	39%	3.1	16	4.6	24	0.0015
A2-2c	2 K	8.0	55%	1.6	5.1	2.7	20	0.0039
A2-5a	2 K	17	43%	2.7	8.9	2.5	21	0.0024
A2-5b	2 K	26	34%	3.2	11	2.3	21	0.0019
A2-5d	2 K	23	40%	3.3	11	2.6	24	0.0022
A2-5b-ANN	2 K	13	44%	2.5	7.1	4.8	21	0.0030
B2	2 K	71	46%	4.3	35	4.6	53	0.0015
B2	30 K	547	7%	11	48	7.1	48	0.0010

ter density. Sample B2 has about the same cluster fraction as sample A2 but with a larger cluster moment. However, at 30 K it has predominantly one type of cluster with $11\mu_B$/cluster. Recently the field-dependent specific heat of Fe_2VAl was successfully treated with two-level Schottky fits.[3] An effective magnetic moment of $3.7\mu_B$ per cluster and a cluster density of 0.0037/f.u. was reported below 8 K. These numbers are comparable to ours, obtained from isothermal magnetization measurements. But we have identified two kinds of SPM clusters with about equal concentration at 2 K.

VII. RESISTIVITY

Resistivities of all our samples are shown in Fig. 5. The resistivity of sample B1 increases with temperature, typical of metallic alloys. Sample A1 has a large residual resistivity, a peak at 18 K, and monotonically decreasing resistivity at higher temperature. The temperature of the peak matches very well with its T_B. The resistivity of sample C has a similar shape but with a much larger residual and overall resistivity. It peaks at 50 K, in accord with the change of its susceptibility with temperature. The increase of resistivity below T_C of sample C and T_B of sample A1 is apparently due to magnetic scattering. For all the samples derived from sample A2, resistivity is marked by a negative TCR and lack of peak structure, in line with the fact that their T_B's are below 2 K. At very low temperature, the resistivities of all A2 samples depart from their almost linear trend. It will be shown later that this upward departure is related to magnetic ordering. Sample B2 has a resistivity almost overlapping that of sample A2-5b.

The fact that two bars, samples A2-5c and A2-5d, from the same bulk sample show resistivity differences of almost a factor of 2 reveals a homogeneity problem, although magnetostatic measurements have yielded fairly consistent results for all A2-derived samples. Various groups have produced quite different resistivity data for arc-melted samples.[1,21,22] The cleaved arc-melted ingots show visible grain boundaries inside the bulk, which might account for part of the resistivity difference. More importantly the antisite disorder in Fe_2VAl is very sensitive to annealing and other conditions under which samples are prepared. It is interesting to note the correlation of the high-temperature susceptibility and the overall magnitude of resistivity in samples A2-2b, 5b, 5d, and 5b-ANN, i.e., the larger the susceptibility the smaller the resistivity. This may be due to the difference in density of states at E_F, which resulted in a concomitant change of Pauli susceptibility and conductivity.

The resistivity measured before annealing at 673 K (sample A2-5b) is smaller than that after annealing (sample A2-5b-ANN). Matsushita *et al.*[21] have established that how a sample of Fe_2VAl is cooled from an anneal at 1073 K will

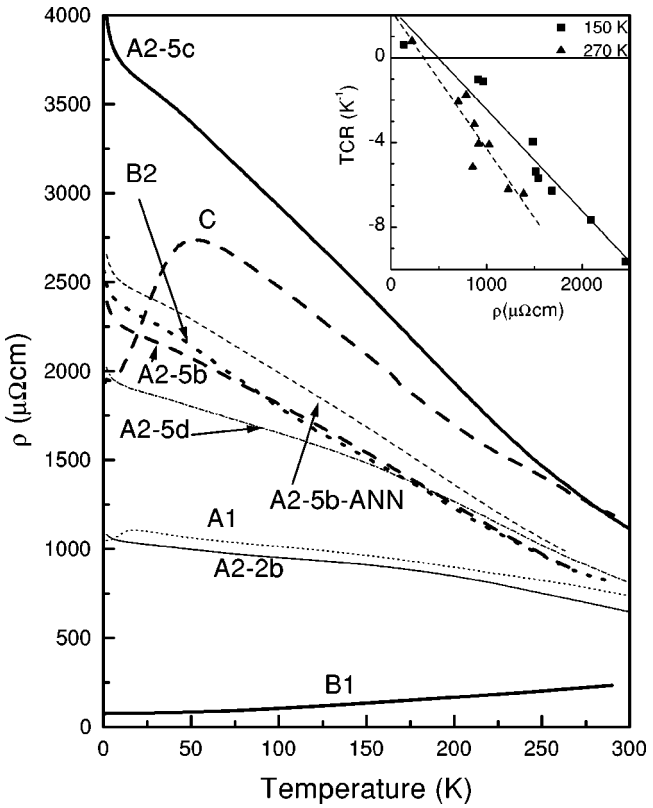

FIG. 5. Resistivity of Fe_2VAl. Inset shows the correlation of TCR and resistivity at $T=150$ K and 273 K. The solid and dashed lines are results of linear regressions.

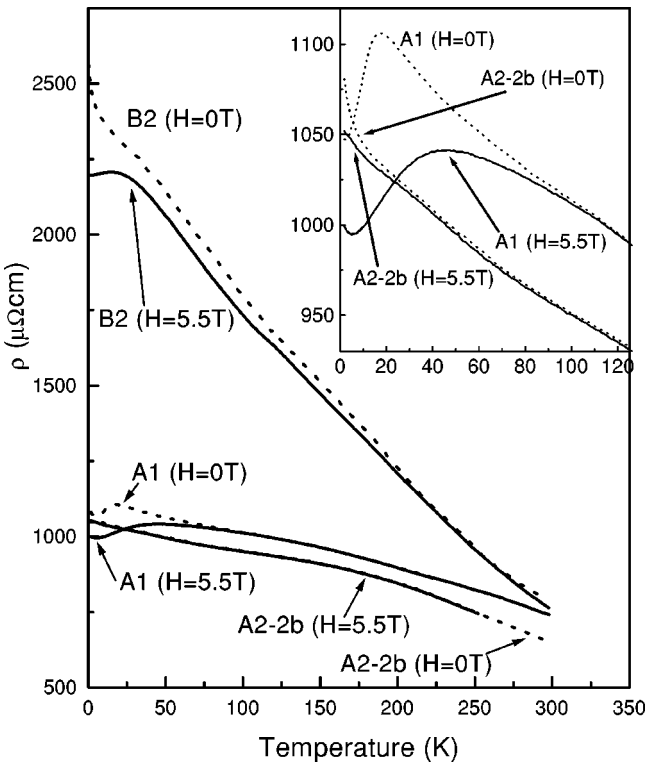

FIG. 6. Magnetic-field dependence of the resistivity of Fe_2VAl. The applied magnetic field is 5.5 T.

determine the magnitude of its resistivity. We want to stress that their anneal is different from our additional low-temperature anneal.

We also measured resistivity vs temperature down to 4 K in a 5.5 T magnetic field (Fig. 6). The resistivities of samples A1, A2-2b, and B2 were all suppressed in the field, but only at low temperature. The peak of sample A1 was shifted to around 40 K and considerably broadened. The suppression of the resistivity of sample A2-2b with applied field indicates the magnetic origin of its upward tail at low temperature. The resemblance of these two sets of data around the bifurcation point, with and without magnetic field, suggests the same kind of residual magnetic ordering, i.e., the magnetic moments of sample A2-2b responded to the applied magnetic field the same way as in sample A1 just above T_B. Sample B2 did not show an appreciable field dependence until around 25 K. In this case, a resistivity maximum was formed, even though without field no maximum was observed. Samples A2, B2, and A1 give a unique set of resistivity data on the magnetic scattering in the presence of external magnetic fields. The suppression of resistivity and the shift or formation of a peak at higher temperature in magnetic fields are both consistent with the field alignment of the spins of SPM clusters, thus making the lattice more ordered for transport and making it harder to thermally break the ferromagnetic alignment of the SPM clusters. The magnetic transformation of samples A2, B2 to sample A1 found here echos our results from the magnetic susceptibility.

Now we try to assess our resistivity data quantitatively, according to possible theoretical models. Several references[1,22] modeled Fe_2VAl as a narrow-gap semiconductor. We fitted our resistivity with $\rho=\rho_{const}+\rho_0\times e^{\Delta E/k_BT}$. Between 240 and 300 K, ΔE was 0.015 eV for samples A1 and A2-2b. For all other samples except B1, the activation energy ΔE was 0.025–0.035 eV. Endo[22] reported a semiconducting gap of 0.07 eV which is close to our gap, $2\Delta E$. However, this gap cannot be taken as exact since the temperature may not be proper to treat the electrons as a nondegenerate gas. The infrared reflectance spectra are also inconsistent with a real semiconducting band gap. In the case of a 0.06-eV band gap, carriers would be frozen at 4 K by the Fermi-Dirac distribution and cause a significant drop of the free-electron concentration. Below 25 K, we can fit the upward resistivity to an energy gap of less than one-tenth of a meV. We dismiss this gap at low temperature as not physically meaningful because the Fermi-Dirac distribution at 2 K easily overwhelms it. Besides, SPM was shown to be related to this upward trend, casting doubt on its electronic origin.

Other physics is possible behind this activation energy of tens of meV. But first, we need to realize that the Boltzmann formulation for conduction is not appropriate for Fe_2VAl. From our FTIR data, the mean free path ($v_F\tau$) for electrons is 27 Å at 4 K and 24 Å at 300 K. With an electron wavelength $2\pi/k_F$ around 34 Å, we cannot use the semiclassical Boltzmann equation and assume the phase memory of electrons is lost in the scattering process. We have to treat this problem using the more general Kubo-Greenwood and multiple-scattering formulations.

Bergmann[23] first pointed out that weak localization through multiple scattering and quantum interference can give an additional contribution to electron localization. This effect is relatively strong when the scattering length is short. Raising the temperature will cause electrons to collide with phonons inelastically, thereby losing coherence, enhancing the conductivity. Weak localization can produce a negative TCR. On the other hand, the application of a magnetic field introduces a relative phase shift of $2e\Delta\phi/\hbar$, which normally destroys the constructive interference and enhances the conductivity. We did not find much change of resistivity with a field of 5.5 T for most of the temperature range in which a negative TCR was observed. We therefore regard weak localization not to be the primary mechanism causing the negative TCR in Fe_2VAl.

Large amounts of disorder in amorphous semiconductors will create mobility edges at the band tails. Beyond the mobility edge, the carrier contribution to the conductivity is nominally zero. The DOS of FeVFeAl calculated from first principles can be split into two subbands above and below E_F due to the crystal field and metallic bonding.[7–9] With a large amount of antisite disorder introduced, a mobility edge on each of the two subbands will be formed right above and below E_F, leaving the states in between localized. The DOS between these two mobility edges will increase with more disorder, filling the void of the pseudogap. The mobility edges will also move toward the centroids of the subbands with more disorder. A rise of temperature will cause more delocalized states above the upper mobility edge and below the lower mobility edge to be involved in the conduction process, giving a negative TCR. This conduction process will probably not cause changes in the Drude term in the IR

due to its short mean scattering time and strong damping. But it is possible that the large density of states at E_F, as seen in the photoemission and specific-heat measurements, comes from localized states.

It is interesting to notice that a negative TCR is prevalent in $Fe_{4-x}Si_x$ for $0 \leqslant x \leqslant 1$,[24] $(Fe_{0.8}M_{0.2})_3Si$ with M=V, Mn, Cr, Ni, Co,[24] $(Fe_{1-x}V_x)_3Si$ for $0 \leqslant x \leqslant 0.2$,[24] $(Fe_{1-x}Co_x)_3Si$ for $0 \leqslant x \leqslant 0.6$,[24] $(Fe_{1-x}V_x)_3Ga$ for $0 \leqslant x \leqslant 0.3$,[25] $(Fe_{1-x}Ti_x)_3Ga$ for $0 \leqslant x \leqslant 0.3$,[25] and $(Fe_{1-x}V_x)_3Al$ for $0 \leqslant x \leqslant 0.35$.[1] Recently Zarek *et al.*[26] reported that Fe_2VAl in a simple cubic lattice also shows a negative TCR between 4.2 and 300 K. With only FeVFeAl in a semimetallic ground state, the negative TCR in these alloys may have little to do with semimetallicity. Mooij[27] studied the transport properties of a number of transition-metal alloys finding that high resistivity with concomitant negative TCR was a ''universal'' property of many. Disordered phases were noted for more effectively creating negative TCR than their ordered counterparts. Putting impurities into pure metals can create a negative TCR. For example, doping up to 33% Al into pure Ti induced a transition from a positive to a negative TCR. The temperature span of this negative TCR was very wide for many alloys. An important conclusion was drawn that the transport properties of these alloys have little dependence on crystal structures or band structures. We think the intrinsic disorder of the Heusler structure is the likely cause of the negative TCR of the above alloys.

Mooij[27] set a room-temperature resistivity of 150 $\mu\Omega$ cm as the universal criterion for the sign of TCR; if the room temperature resistivity of a sample is larger than this value it is likely to have a negative TCR. Later, Tsuei[28] collected more data and concluded that Mooij's criterion was based on too small a data set and that the ''universal criterion'' of 150 $\mu\Omega$ cm is *not* universal. He also argued that the nonuniversality of the Mooij correlation is mostly attributed to the competition between the quantum-mechanical effects of incipient localization and classical Boltzmann electron transport. However, there is still a unique and monotonic correlation between the TCR and resistivity for a specific disordered metallic system. The crossover resistivity ρ_c from negative to positive TCR is not universal to all materials, but dependent upon the individual material characteristics. ρ_c is given by[28]

$$\rho_c = \rho_B(0)\left[1 - \frac{3}{(k_F l_e)^2} + \frac{6.75}{(k_F l_e)^4}\right]^{-1},$$

where

$$\rho_B(0) = \frac{3\pi^2\hbar}{e^2 k_F^2 l_e},$$

the Boltzmann resistivity at $T=0$ K and l_e is the elastic mean free path. Since actual numerical analysis[28] reveals a fairly linear relation between the TCR and the resistivity near and below zero TCR, we plot our samples' TCR-vs-resistivity at 150 and 273 K in the inset of Fig. 5. From linear regression we get $\rho_c = 492$ and 342 $\mu\Omega$ cm at 150 and 273 K, respectively. Both are larger than the value suggested by Mooij. If we use $k_F = 1.8 \times 10^7$ cm^{-1} from our FTIR analysis, l_e is 11.4 Å at 150 K and 14.2 Å at 273 K. These values are about half the l_e's obtained from the FTIR data analysis. Since we did not measure a series of samples with various levels of disorder, we could not claim that these values have a firm physical meaning. Nevertheless, this analysis gives us at least a clear understanding that the disorder in Fe_2VAl alloys plays an important role in many physical properties.

Without the interference of magnetic ordering in Fe_2VAl samples at low temperature, the residual resistivity (ρ_{RES}) would be the almost-linearly-temperature-dependent resistivity extended to 0 K. Understanding ρ_{RES} in these Heusler alloys, without the complication due to the anomalously large magnetic scattering[24,25] present, should shed some light on this negative TCR. The ρ_{RES} of $(Fe_{1-x}V_x)_3Ga$, $(Fe_{1-x}V_x)_3Si$, and $(Fe_{1-x}V_x)_3Al$ are plotted in Fig. 7. The data points have been taken from Ref. 1 for $(Fe_{1-x}V_x)_3Al$, Refs. 24 and 29 for $(Fe_{1-x}V_x)_3Si$, and Refs. 22 and 25 for $(Fe_{1-x}V_x)_3Ga$.

Work on $Fe_3Si_{1-x}Al_x$ (Ref. 30) yielded considerable insight on the effect of disorder in Heusler alloys. It was found that the Al-Fe site disorder can be assumed to be proportional to the amount of Fe_3Al present in Fe_3Si, resulting in a linear relation of ρ_{RES} and x. The Si-Al disorder scattering has a parabolic dependence on x, vanishing at $x=0$ and $x=1$. In Fig. 7 the ρ_{RES} of $(Fe_{1-x}V_x)_3Si$ and $(Fe_{1-x}V_x)_3Ga$ can be similarly understood in terms of Fe_3Si, Fe_2VSi, Fe_3Ga, and Fe_2VGa. The resistivity induced by the Fe-V disorder in these two series can be estimated to be of the order of 100 $\mu\Omega$ cm. The distortion of the parabolic shape in $(Fe_{1-x}V_x)_3Ga$ is obvious, with the peak position moving to $x=0.25$. The gross shape of ρ_{RES} vs x of $(Fe_{1-x}V_x)_3Al$ seems to contradict the above simple model of antisite disorder. However, in the following we shall see that the ρ_{RES} of $(Fe_{1-x}V_x)_3Al$ can be approximated as well by the homogeneous mixing of Fe_3Al and Fe_2VAl with intrinsic disorder in both compounds.

The linear dependence of ρ_{RES} on x between end-point compounds has a root in percolation theory. When two media are mixed homogeneously and each makes a closed circuit, we have in effect two resistors in parallel. Assuming

$$R_1 = \frac{\rho_1 l}{xA} \quad \text{and} \quad R_2 = \frac{\rho_2 l}{(1-x)A},$$

one gets

$$\rho_{tot}(x) = \frac{\rho_2\rho_1}{\rho_1 + (\rho_2 - \rho_1)x},$$

where x is the volume fraction of the phase with resistivity ρ_1. When ρ_1 and ρ_2 are not very different, $\rho_{tot}(x)$ is almost a straight line connecting the end points. This is indeed the case in $Fe_3Si_{1-x}Al_x$, $(Fe_{1-x}V_x)_3Si$, and $(Fe_{1-x}V_x)_3Ga$. But when there is a large difference between ρ_1 and ρ_2, as in the case of Fe_3Al and Fe_2VAl, the above formula gives an upward curvature, similiar to our experimental data. Shown in the inset of Fig. 7 is the experimental ρ_{RES} with that from percolation mixing of end-point compounds subtracted. It is

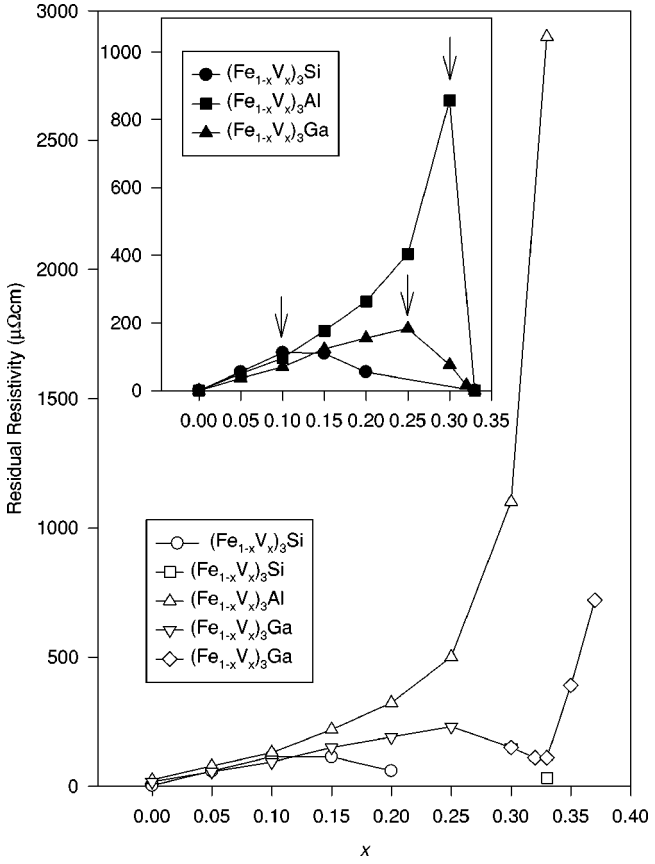

FIG. 7. Residual resistivities of Heusler alloys $(Fe_{1-x}V_x)_3Ga$ (∇: Ref. 25; $\diamond$: Ref. 22), $(Fe_{1-x}V_x)_3Si$ ($\bigcirc$: Ref. 24; $\square$: Ref. 29), and $(Fe_{1-x}V_x)_3Al$ ($\triangle$: Ref. 1). The inset shows residual resistivities with contributions from percolation mixing subtracted.

observed that the difference curve for $(Fe_{1-x}V_x)_3Al$ has a parabolic shape with even more distortion than that for $(Fe_{1-x}V_x)_3Ga$. We think the shift of the ''parabolic'' peak is probably related to stronger multiple scattering due to electron localization. Although it is very crude to assume that $(Fe_{1-x}V_x)_3Al$ is a simple mixture of Fe_3Al and Fe_2VAl with Fe-V disorder considered additionally, there are experimental indications of a continuous ferromagnetism-to-SPM transition from Fe_3Al to Fe_2VAl.[5]

VIII. SUMMARY

Through our investigation, Heusler-like Fe_2VAl is regarded as having mostly the FeVFeAl structure but with severe antisite disorder. This leads to large deviations of physical properties from the theoretical speculations based on the ideal FeVFeAl structure. Magnetically, SPM clusters form out of antisite disorder. However, not all antisite disorder results in the formation of SPM clusters. If we assume each disordered FeVFeAl formula unit contributes an average of $2\mu_B$, with the available data on saturation magnetization and ferromagnetic coupling assumed, there are about only 1–2 % of the formula units in SPM states. The moments of Fe atoms in other disordered cells are probably locked in a spin-glass or antiferromagnetic state with no average moment.

The electronic structure of Fe_2VAl is not strongly perturbed by antisite disorder except near E_F. The DOS can be decomposed into two parts. The FeVFeAl phase has a DOS predicted from first-principles calculations. This phase is the origin of the observed Drude conductivity. The disordered phase has a large DOS near E_F and these states are localized. Away from E_F, there are delocalized electrons and holes on the far sides of the mobility edges. With E_F falling in the gap of the DOS of itinerant carriers, the mobile free-carrier density is small and has little temperature dependence. However, with an increase of temperature, more delocalized carriers from the disordered phase are involved in the conduction process, giving a negative TCR. The very large ρ_{RES} of Fe_2VAl is due to the low density of carriers in the ordered phase and the freezing of delocalized carriers in the disordered phase. With most of the DOS at E_F from localized states, the intensity of Fermi-edge photoemission[1] and the specific-heat coefficient are enhanced in Fe_2VAl relative to the ordered phase. Recent resonant photoemission experiments found that the partial DOS calculated from first principles depicts the valence band of Fe_2VAl very well, except near E_F.[2] This finding is in qualitative agreement with our assignment of the DOS as well. We found no evidence in these samples for heavy-fermion behavior.

We can make a simple comparison of the electronic properties of Fe_2VAl and amorphous Si. With similar DOS's, the negative TCR in Fe_2VAl results from the same physics that caused the resistivity to drop with increasing temperature in amorphous Si. The optical-absorption edge in amorphous Si is not very sharp and falls off exponentially according to Urbach's rule because of the transitions from and to the tail states. Optical conductivity of similar shape near the onset of interband absorption is also observed in Fe_2VAl.

ACKNOWLEDGMENTS

We would like to thank Eva Talik for providing us the Czochralski samples and preprint of Ref. 26, R. Modler and J. E. Ostenson for part of the resistivity and magnetization measurements, and P. C. Canfield and B. N. Harmon for helpful discussions. Ames Laboratory is operated for the U.S. Department of Energy by Iowa State University under Contract No. W-7405-Eng-82. This work was supported by the Director for Energy Research, Office of Basic Energy Science. One of us (J.Y.R.) was also supported by the Korea Science and Engineering Foundation through Project No. 97-0702-01-01-3.

*On leave from Department of Physics, Hoseo University, Asan, Choongnam 336-795, Korea.

[1] Y. Nishino, M. Kato, S. Asano, K. Soda, M. Hayasaki, and U. Mizutani, Phys. Rev. Lett. **79**, 1909 (1997).

[2] K. Soda, T. Takeuchi, Y. Yanagida, U. Mizutani, M. Kato, Y. Nishino, A. Sekiyama, S. Imada, S. Suga, T. Matsushita, and Y. Saito, Jpn. J. Appl. Phys., Suppl. **38**, 496 (1999).

[3] C.S. Lue, J.H. Ross, Jr., C.F. Chang, and H.D. Yang, Phys. Rev.

B **60**, R13 941 (1999).
[4] M. Kato, Y. Nishino, U. Mizutani, and S. Asano, J. Phys.: Condens. Matter **12**, 1769 (2000).
[5] E. Popiel, M. Tuszynski, W. Zarek, and T. Rendecki, J. Less-Common Met. **146**, 127 (1989).
[6] G.Y. Guo, G.A. Botton, and Y. Nishino, J. Phys.: Condens. Matter **10**, L119 (1998).
[7] D.J. Singh and I.I. Mazin, Phys. Rev. B **57**, 14 352 (1998).
[8] R. Weht and W.E. Pickett, Phys. Rev. B **58**, 6855 (1998)
[9] A. Bansil, S. Kaprzyk, P.E. Mijnarends, and J. Tobola, Phys. Rev. B **60**, 13 396 (1999).
[10] E. Talik, J. Szade, J. Heimann, A. Winiarski, A. Winiarska, K. Majewska, and A. Chelkowski, J. Cryst. Growth **102**, 187 (1990).
[11] D.E. Okpalugo, J.G. Booth, and C.A. Faunce, J. Phys. F: Met. Phys. **15**, 681 (1985).
[12] G. Nolze (private communication).
[13] W.G. Fateley, F.R. Dollish, N.T. McDevitt, and F.F. Bentley, *Infrared and Raman Selection Rules for Molecular and Lattice Vibrations: The Correlation Method* (John Wiley & Sons, New York, 1972).
[14] A.J. Bradley and A.H. Jay, Proc. R. Soc. London, Ser. A **136**, 210 (1932).
[15] B. Fultz, T.A. Stephens, W. Sturhahn, T.S. Toellner, and E.E. Alp, Phys. Rev. Lett. **80**, 3304 (1998).
[16] H. Okamura, J. Kawahara, T. Nanba, S. Kimura, K. Soda, U. Mizutani, Y. Nishino, M. Kato, I. Shimoyama, H. Miura, K. Fukui, K. Nakagawa, H. Nakagawa, and T. Kinoshita, Phys. Rev. Lett. **84**, 3674 (2000).
[17] Ye Feng, C. Ambrosch-Draxl, J.M. Park, A.J. Sievers, C.G. Olson, and D.W. Lynch (unpublished).
[18] Z. Schlesinger, Z. Fisk, H.-T. Zhang, M.B. Maple, J.F. DiTusa, and G. Aeppli, Phys. Rev. Lett. **71**, 1748 (1993).
[19] A. Damascelli, K. Schulte, D. van der Marel, and A.A. Menovsky, Phys. Rev. B **55**, R4863 (1997).
[20] M.A. Chernikov, L. Degiorgi, E. Felder, S. Paschen, A.D. Bianchi, H.R. Ott, J.L. Sarrao, Z. Fisk, and D. Mandrus, Phys. Rev. B **56**, 1366 (1997).
[21] A. Matsushita and Y. Yamada, J. Magn. Magn. Mater. **196-197**, 669 (1999).
[22] K. Endo, H. Matsuda, K. Ooiwa, M. Iijima, T. Goto, K. Sato, and I. Umehara, J. Magn. Magn. Mater. **177-181**, 1437 (1998).
[23] G. Bergmann, Phys. Rev. B **28**, 2914 (1983).
[24] Y. Nishino, S. Inoue, S. Asano, and N. Kawamiya, Phys. Rev. B **48**, 13 607 (1993).
[25] N. Kawamiya, Y. Nishino, M. Matsuo, and S. Asano, Phys. Rev. B **44**, 12 406 (1991).
[26] W. Zarek, E. Talik, J. Heimann, M. Kulpa, A. Winiarska, and M. Neumann, J. Alloys Compd. **297**, 53 (2000).
[27] J.H. Mooij, Phys. Status Solidi A **17**, 521 (1973).
[28] C.C. Tsuei, Phys. Rev. Lett. **57**, 1943 (1986); C.C. Tsuei, in *Anderson Localization*, edited by T. Ando and H. Fukuyama (Springer-Verlag, Heidelberg, 1988), p. 143.
[29] K. Endo, H. Matsuda, K. Ooiwa, and K. Itoh, J. Phys. Soc. Jpn. **64**, 2329 (1995).
[30] W.B. Muir, J.I. Budnick, and K. Raj, Phys. Rev. B **25**, 726 (1982).